

ARTICLE

Open Access

Tailoring spin mixtures by ion-enhanced Maxwell magnetic coupling in color-tunable organic electroluminescent devices

Junwei Xu^{1,2}, Yue Cui^{1,3}, Gregory M. Smith^{1,2,9}, Peiyun Li^{2,4}, Chaochao Dun^{1,2}, Linqi Shao^{1,5}, Yang Guo^{1,6,7}, Hongzhi Wang^{6,7}, Yonghua Chen⁸ and David L. Carroll^{1,2}

Abstract

In this work, we show that the spin dynamics of excitons can be dramatically altered by Maxwell magnetic field coupling, together with an ion-enhanced, low-internal-splitting-energy organic semiconducting emitter. By employing a unique, alternating current (AC)-driven organic electroluminescent (OEL) device architecture that optimizes this magnetic field coupling, almost complete control over the singlet-to-triplet ratio (from fluorescent to phosphorescent emission in a single device) is realized. We attribute this spin population control to magnetically sensitive polaron–spin pair intersystem crossings (ISCs) that can be directly manipulated through external driving conditions. As an illustration of the utility of this approach to spin-tailoring, we demonstrate a simple hybrid (double-layer) fluorescence–phosphorescence (F–P) device using a polyfluorene-based emitter with a strong external Zeeman effect and ion-induced long carrier diffusion. Remarkable control over de-excitation pathways is achieved by controlling the device-driving frequency, resulting in complete emission blue–red color tunability. Picosecond photoluminescence (PL) spectroscopy directly confirms that this color control derives from the magnetic manipulation of the singlet-to-triplet ratios. These results may pave the way to far more exotic organic devices with magnetic-field-coupled organic systems that are poised to usher in an era of dynamic spintronics at room temperature.

Introduction

In today's current-driven organic electroluminescence (OEL) devices, of which organic lighting diodes are a subset, free charges are injected through metal contacts into an organic semiconductor, where they can recombine into electron–hole (e–h) pairs and decay to emit photons^{1,2} (or they can be transported through the layer without interacting). Quantum statistics dictates that the fraction of spin pairs that are formed in the spin-triplet excited state is generally fixed at 75%. The spin-singlet states make up the remaining 25% of the excited-state

population^{3,4}. This means that when re-combining injected spin–1/2 polaron–spin pairs for EL, three of every four possible spin combinations will be triplets (with nonradiative or infrared decay routes), and one of the four will be a singlet (fluorescent emission). This has prompted the use of triplet scavenging dyes that resonantly transfer the triplet energy to a metal complex (e.g., Pt, Os, Ir, Au, Pd, or Ru) with strong L–S coupling^{5–7}, which allows phosphorescent emission and higher device efficiency.

The resonant transfer of energy is useful for lighting and display applications. However, owing to the lifetimes involved in triplet transfer or decay, the limits on the current flux and dye concentrations due to co-localization of triplet energy, and the subsequent quenching, among other considerations, resonant energy transfer does not address the issues that spin-triplets cause for high-performance light-emitting applications. These potential

Correspondence: David L. Carroll (carroldl@wfu.edu)

¹Center for Nanotechnology and Molecular Materials, Wake Forest University, Winston-Salem, NC 27109, USA

²Department of Physics, Wake Forest University, Winston-Salem, NC 27106, USA

Full list of author information is available at the end of the article.

© The Author(s) 2018



Open Access This article is licensed under a Creative Commons Attribution 4.0 International License, which permits use, sharing, adaptation, distribution and reproduction in any medium or format, as long as you give appropriate credit to the original author(s) and the source, provide a link to the Creative Commons license, and indicate if changes were made. The images or other third party material in this article are included in the article's Creative Commons license, unless indicated otherwise in a credit line to the material. If material is not included in the article's Creative Commons license and your intended use is not permitted by statutory regulation or exceeds the permitted use, you will need to obtain permission directly from the copyright holder. To view a copy of this license, visit <http://creativecommons.org/licenses/by/4.0/>.

but unrealized applications include the electrically stimulated organic laser⁸, the photonic spin valve, organically based optical computing paradigms, and telecommunications. Without more complete spin-population control, it is unlikely that any of these technologies will be realized using the organic platform⁹.

Until recently, there did not seem to be any way to beat the statistics of this problem. However, in 2007¹⁰, a hint was provided experimentally in the negative magnetoresistance of an organic semiconductor device. The typical 75%:25% ratio of triplets to singlets is not maintained when external, static magnetic fields are present. This has been attributed to a spin remixing in the polaron–spin pairs that is typically found in organic systems^{10–13}. Simply, the external magnetic field can perturb the coherent relationship between electron and hole spin precessions^{14–16}. Therefore, an enhanced singlet-related emission can be observed in a fluorescent semiconducting polymer that has a low internal splitting energy or a strong Zeeman effect. However, phosphorescent organic semiconductors do not exhibit the spin remixing property in the external magnetic field since the heavy metal atom can significantly raise the internal splitting energy of the organic compound¹³. Moreover, in magnetically coupled OEL devices, the redistribution of singlet and triplet e–h pairs can give rise to a significant change in the electrical current in the semiconductor through dissociation^{17–21} and charge reaction^{22–25} (Figure S1). However, the key to utility is to extend this control over the spin populations.

By utilizing the magnetic field spin remixing phenomena, in our present work, a novel device architecture is optimized to self-couple the time-dependent Maxwell field into the ion-assisted emitter. With a suitable choice of emitters for this structure, a high color contrast in spin-state ratios for a single compact device structure can be achieved. Color-tunable pixels have a unique potential for use in ultra-high-resolution information displays^{26,27} since they allow for an optimal fill factor and impart further momentum toward realizing high-definition micro-displays. One of most common color-tuning strategies is to induce a voltage-dependent color shift via a spatial shift of the recombination zone or exciton redistribution within a multi-layered device^{28,29}. However, this leads to inevitable brightness changes and quenching in the high fields, making the voltage-dependent color-tunable devices more difficult and expensive to commercialize. Another method seen in the literature is to stack two or three color-independent OEL segments into a tandem device^{27,30}. However, stacking tandem EL structures requires complicated multiple thin film deposition and designs of electrical power for multiple electrodes.

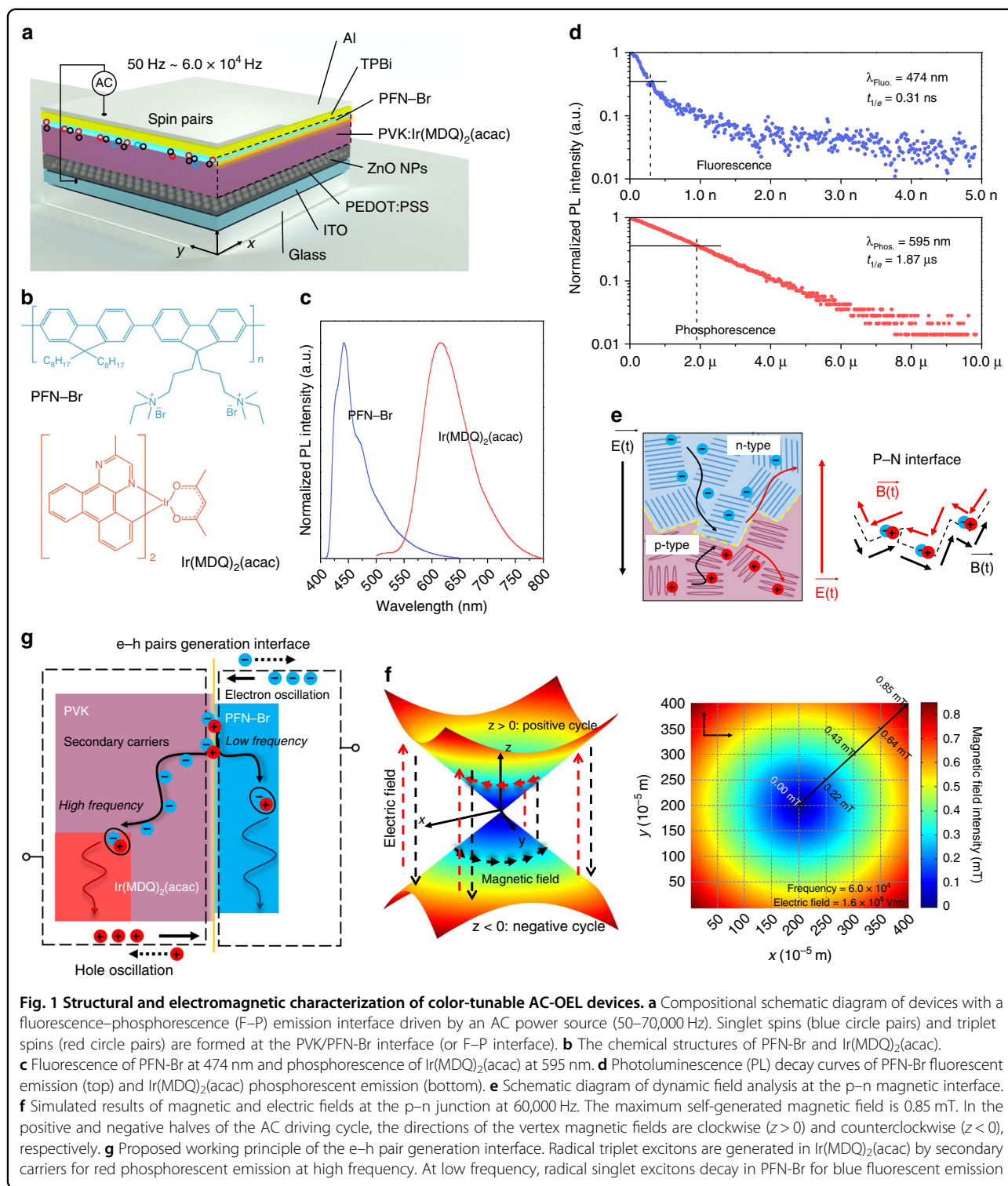
Here a color-change hybrid alternating current (AC)-driven OEL device is driven with a high-frequency AC electric field. This yields a Maxwell AC magnetic field that

is coupled to the organic emitter, namely, a p–n-emitting interface. The internal AC magnetic field allows the manipulation of the ratio between singlet and triplet e–h pairs in an n-type fluorescent material by suppressing intersystem crossing (ISC) to generate diffusive secondary carriers. Then these ion-enhanced secondary carriers produce triplet-spin excitons in a proximal phosphorescent organic matrix. In the magnetically coupled fluorescence–phosphorescence (F–P) hybrid OEL device, we successfully shifted the CIE coordinates of the radiative output from (0.23, 0.34) to (0.53, 0.40) by manipulating the driving frequency from 50 to 60,000 Hz with no significant brightness change.

Results

Our device architecture (Fig. 1a) borrows from the “gated” AC-OEL structure that were introduced recently in the literature³¹. In this case, however, the gated structure is coupled to a bilayer organic emitter consisting of [poly(N-vinylcarbazole) (PVK):bis(2-methylbenzo[f,h]quinoxaline) (acetylacetonate)iridium(III) (Ir(MDQ)₂(acac)) and poly[(9,9-bis(3'-((N,N-dimethyl)-N-ethylammonium)-propyl)-2,7-fluorene)-alt-2,7-(9,9-dioctylfluorene)] (PFN-Br)]. Surface morphology analyses of PVK:Ir(MDQ)₂(acac) and PFN-Br emissive layers are performed via atomic force microscopy (AFM); the obtained images can be found in Figure S2. As in an earlier work³², the carrier gate layer was composed of [poly(3,4-ethylenedioxythiophene) polystyrene sulfonate (PEDOT:PSS) that was loaded with ZnO nanoparticles (NPs)] and the electron-transporting layer was [2,2',2''-(1,3,5-benzotriptyl)-tris(1-phenyl-1-H-benzimidazole) (TPBi)]. The two conductive electrodes were indium tin oxide (ITO) and aluminum (Al). The chemical structures of the emitters, namely, PFN-Br and Ir(MDQ)₂(acac), are listed in Fig. 1b. With 365 nm ultraviolet (UV) excitation, PFN-Br and Ir(MDQ)₂(acac) show strong fluorescent and phosphorescent luminescence peaks at 474 and 585 nm, respectively (as shown in Fig. 1c). The lifetimes of short-lived blue fluorescence and long-lived red phosphorescence are given in Fig. 1d for 0.31 ns and 1.87 μs, respectively. With ZnO NPs (~35 nm in diameter) gating the interface of ITO/PEDOT:PSS, injected charges can be efficiently manipulated under the forward and reverse biases of AC cycles^{32–34}. The AC-OEL devices are driven by a sinusoidal voltage with a wide frequency range from 50 Hz, which causes the gate to allow bi-polar injection and the device to act like a diode, to 60,000 Hz, at which most light is created by field-generated polarons/excitons with little diffusive transport in the active volume of the emitter. The operating mechanism of AC-OEL devices is described in detail in Supplemental Information.

PFN-Br is a high-performance ionized electron-transporting polymer^{35,36} with an electron mobility of



$1.41 \times 10^{-7} \text{ cm}^2/\text{V}\cdot\text{s}$, and PVK is a typical p-type semiconductor with a hole mobility on the order of $1.0 \times 10^{-6} \text{ cm}^2/\text{V}\cdot\text{s}$. Thus electrons and holes are transferred and interact at the PVK/PFN-Br interface under an external electric field. The time for accumulation at this interface

depends on the driving frequency. However, as already noted at high frequencies, the gate of the system allows only for field-generated carrier injection into the emitting volume, while at lower frequencies the gate allows for direct injection from the contacts. Nevertheless, both

conditions result in charge drift toward the interface (illustrated in Fig. 1e). The electrons and holes are transferred to the heterointerface in the positive cycle of the AC electric field and drift along the opposite direction under the reverse bias^{37–39}. Therefore, the time-dependent electric field generates an interfacial magnetic field at the PVK:Ir(MDQ)₂(acac)/PFN-Br heterointerface according to Maxwell's equations. In an ideal case, the pixel dimension is $4 \times 4 \text{ mm}^2$, which is significantly larger than its thickness ($\sim 300 \text{ nm}$); hence, it is reasonable to ignore fringing effects (the infinite-area parallel-plate-capacitor assumption). Via engaging a high-frequency driving (60,000 Hz) under a strong AC electrical field ($1.6 \times 10^8 \text{ V/m}$), the temporal and spatial characteristics of the internal magnetic field are shown in Fig. 1f. The upper and lower half-planes represent the opposite “clock directions” of the magnetic field in the positive and negative halves of an AC cycle. The amplitude of the magnetic field is estimated to be approximately 0.85 mT. More details can be found in Supplemental Information, along with simulation results with various frequencies in Figure S3. The dynamic revolution of the magnetic field is shown in Movie S1.

The heterointerface also plays the role of an e–h pair recombination zone for hot carrier injection, as shown in the energy-level diagram in Fig. 1g. These e–h pairs not only move in the applied electric field but also experience the induced magnetic field. The device shows a blue emission (in Figure S4) due to the PFN-Br fluorescence at near-DC driving (50 Hz) since the dissociation rate of e–h pairs is negligible in the absence of an induced magnetic field ($< 0.00005 \text{ mT}$). When this internal AC magnetic field is of the same order as the nuclear hyperfine field ($\sim 1 \text{ mT}$), ISC suppression should occur¹¹ and this would naturally lead to singlet-spin e–h pair accumulation. Many secondary carriers are produced in PFN-Br through the magnetically mediated dissociation of the e–h pairs. The secondary charges diffuse to nearby Ir(MDQ)₂(acac) sites, which yields decay of triplet-state excitons, as shown in Figure S4. There is no significant position shift of the recombination zone in the device, as shown in Figure S5. Thus, as illustrated in Fig. 1g, in the low-frequency driving regime (50–1000 Hz), hot carrier injection is the main mechanism for fluorescent excitons in PFN-Br. In the high-frequency regime (30,000–70,000 Hz), the high-intensity AC magnetic field at the F–P interface populates singlet-excited e–h pairs mostly via ISC suppression, which leads to secondary carriers. The secondary carriers exist in the form of bonded electrons in the PFN-Br polymer matrix, more specifically, with Br atoms, which are strong electron acceptors. The charged Br ions significantly improve the carrier diffusion length⁴⁰, resulting in negative charges moving across the interfacial energy barrier. Consequently, the secondary carriers are

transferred to Ir(MDQ)₂(acac) for red phosphorescent emission. For the same reason, the charged movable Br ions greatly facilitate magnetic field current, even under very subtle magnetic intensity with non-ionized polymer, which normally requires over hundreds of mT⁴¹. More discussion is presented in supplementary information.

Figure 2a, b show the evolution of the device's EL spectrum with increasing electric field at low and high frequencies. At the frequency of 50 Hz, there are trivial spectral shifts in Fig. 2a when the applied voltage varies from 15.4 to 20.4 V; however, no phosphorescence is observed. This is attributed to the dominant hot carrier injections, as shown in Fig. 2c. Electrons and holes are injected in the positive halves of voltage cycles while no current injection occurs in the reverse bias. Hot carrier injection is strongly related to the 474-nm-wavelength fluorescence.

For 60,000 Hz (secondary-carrier-related), as shown in Fig. 2b, the EL intensity of the fluorescent emission at 474 nm is nearly identical to that observed at 50 Hz. However, the 595 nm phosphorescent peak grows as the external electric field increases. Examining current transients in Fig. 2d, the total current density is the sum of the root-mean-square (RMS) values of the sinusoidal waveform and the direct current (DC) offset ($J_{\text{tot}} = J_{\text{dc}} + J_{\text{sine}}$; the method used for current component determination can be found in Supporting Information). Under the lower voltage of 17.9 V, the DC current density and RMS sine current density are 60.2 and 36.6 mA/cm², respectively. Compared to higher voltages (18.9, 19.8, 20.6, 21.5, and 22.0 V), the DC current densities are dramatically increased to 82.3, 114.9, 138.5, 164.1, and 184.6 mA/cm² while relatively constant RMS sinusoidal currents of 37.8, 39.4, 42.1, 43.7, and 45.2 mA/cm², respectively, are observed. We suggest that the tremendous enhancement of the secondary charge current produces the growth of the 595-nm-wavelength phosphorescence.

In addition, $J_{\text{rms}}-L-V_{\text{rms}}$ characteristics at low frequency (50 Hz) and high frequency (60,000 Hz) are shown in Fig. 2e, in which the maximum brightnesses, namely, 360 cd/m² in blue and 600 cd/m² in red, are of the order that is necessary for devices for personal display use. Figure 2f shows the relation between J_{rms} and L at the frequencies of 50 Hz and 60 kHz. The 50 Hz curve is fitted by a linear function, which has been widely demonstrated in the standard DC-driven organic light-emitting diodes (OLEDs). The linear fit strongly suggests that the exciton concentration inside the device remains below the level at which multi-exciton effects are dominant, such as Auger, quenching, and dissociation. In contrast, the 60 kHz curve can be fitted not by a linear function but by a first-order exponential function, which indicates an improved exciton recombination efficiency, which rules out the Auger recombination and quenching effects. The exponential

line fits the data in both the high- and low-current regimes, which suggests that the phosphorescent exciton recombination efficiency is independent of the exciton density. These triplets are again generated by the free carriers from the e-h dissociation promoted by the AC-magnetic-field-assisted ISC suppression. Therefore, rather

than the injection efficiency, the AC field is the main factor that impedes the singlet-to-triplet ISC. In consequence, a higher power efficiency is achieved at 60,000 Hz (1.5 lm/W; details are shown in Figure S6).

The luminance–frequency characteristics of the color-tunable AC-OEL device are shown in Fig. 3a. The total

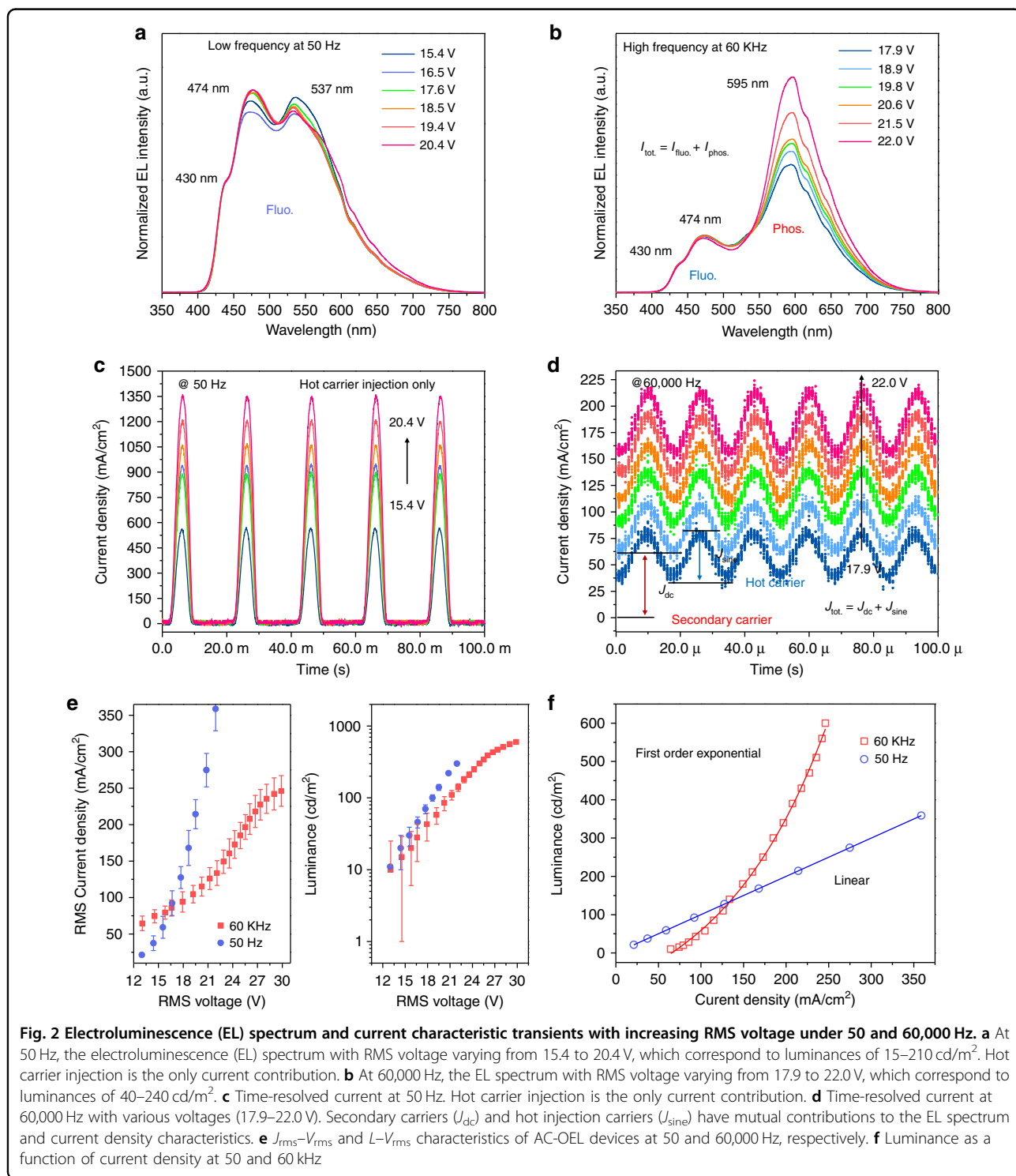
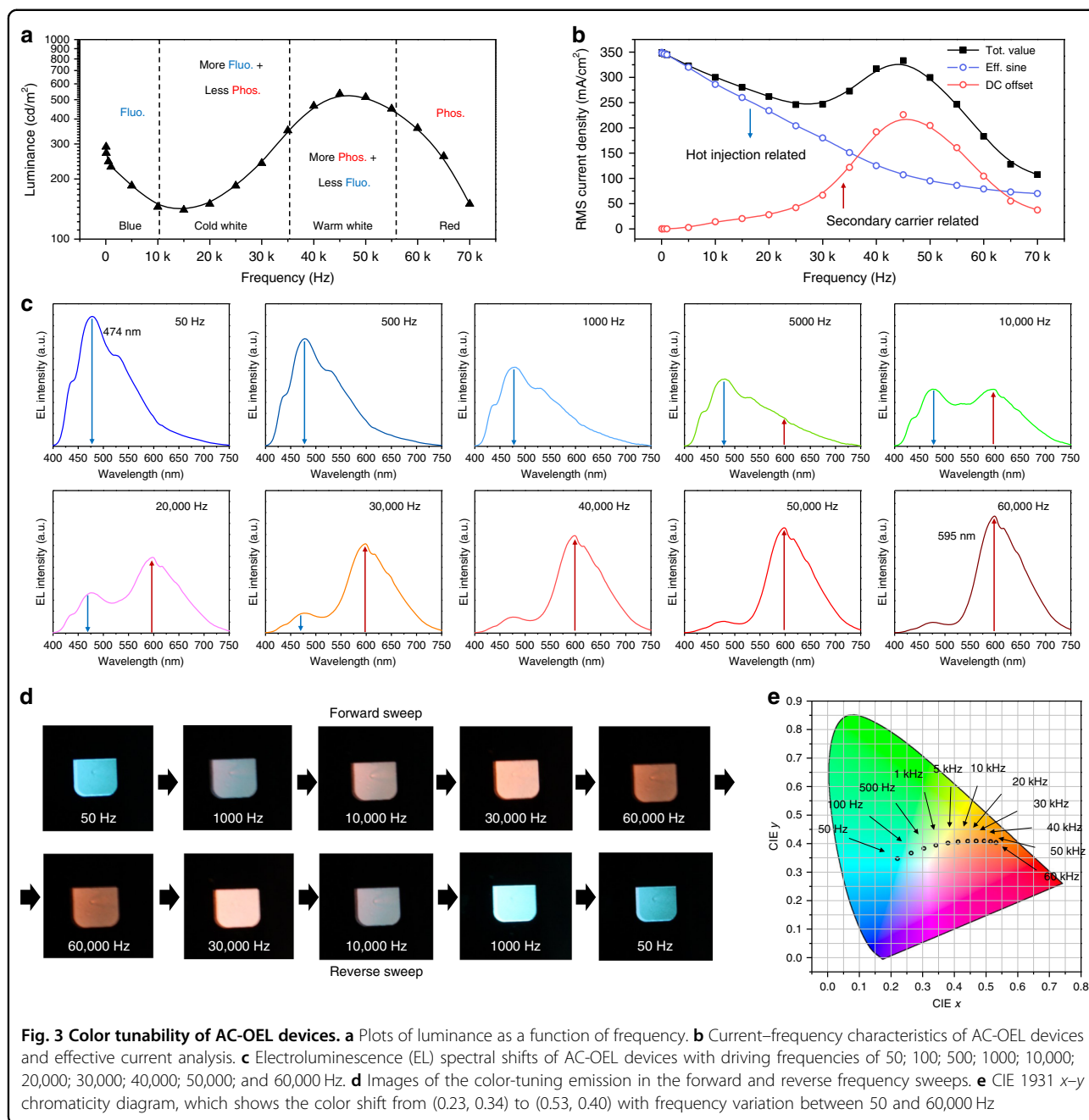


Fig. 2 Electroluminescence (EL) spectrum and current characteristic transients with increasing RMS voltage under 50 and 60,000 Hz. **a** At 50 Hz, the electroluminescence (EL) spectrum with RMS voltage varying from 15.4 to 20.4 V, which correspond to luminances of 15–210 cd/m². Hot carrier injection is the only current contribution. **b** At 60,000 Hz, the EL spectrum with RMS voltage varying from 17.9 to 22.0 V, which correspond to luminances of 40–240 cd/m². **c** Time-resolved current at 50 Hz. Hot carrier injection is the only current contribution. **d** Time-resolved current at 60,000 Hz with various voltages (17.9–22.0 V). Secondary carriers (J_{dc}) and hot injection carriers (J_{sine}) have mutual contributions to the EL spectrum and current density characteristics. **e** J_{rms} – V_{rms} and L – V_{rms} characteristics of AC-OEL devices at 50 and 60,000 Hz, respectively. **f** Luminance as a function of current density at 50 and 60 kHz



emission of the device shifts between the fluorescent and phosphorescent contributions, whereas the luminance is relatively stable over the frequency. Corresponding to the F–P shift, the frequency characteristics are also shown with respect to current density in Fig. 3b. Analyzing the low-frequency regime (<1000 Hz) first, low frequencies lead to dominant blue fluorescence since, as we suspected, the device under low-frequency driving acts more like a carrier-injection-type diode in the forward and reverse biases (Figure S7).

At higher frequencies (>10,000 Hz), the current density consists of a sinusoidal contribution and a DC offset (see Figure S7), essentially reflecting both the displacement of the direct current injection and the secondary charge current, respectively. In Fig. 3b, the DC offset component of the current through the device starts at a very low level (13.8 mA/cm²) at 10,000 Hz and increases to 226.1 mA/cm² at 45,000 Hz. In contrast, the RMS value of the sinusoidal component of the current waveform drops from 286.1 mA/cm² at 10,000 Hz to 106.8 mA/cm² at

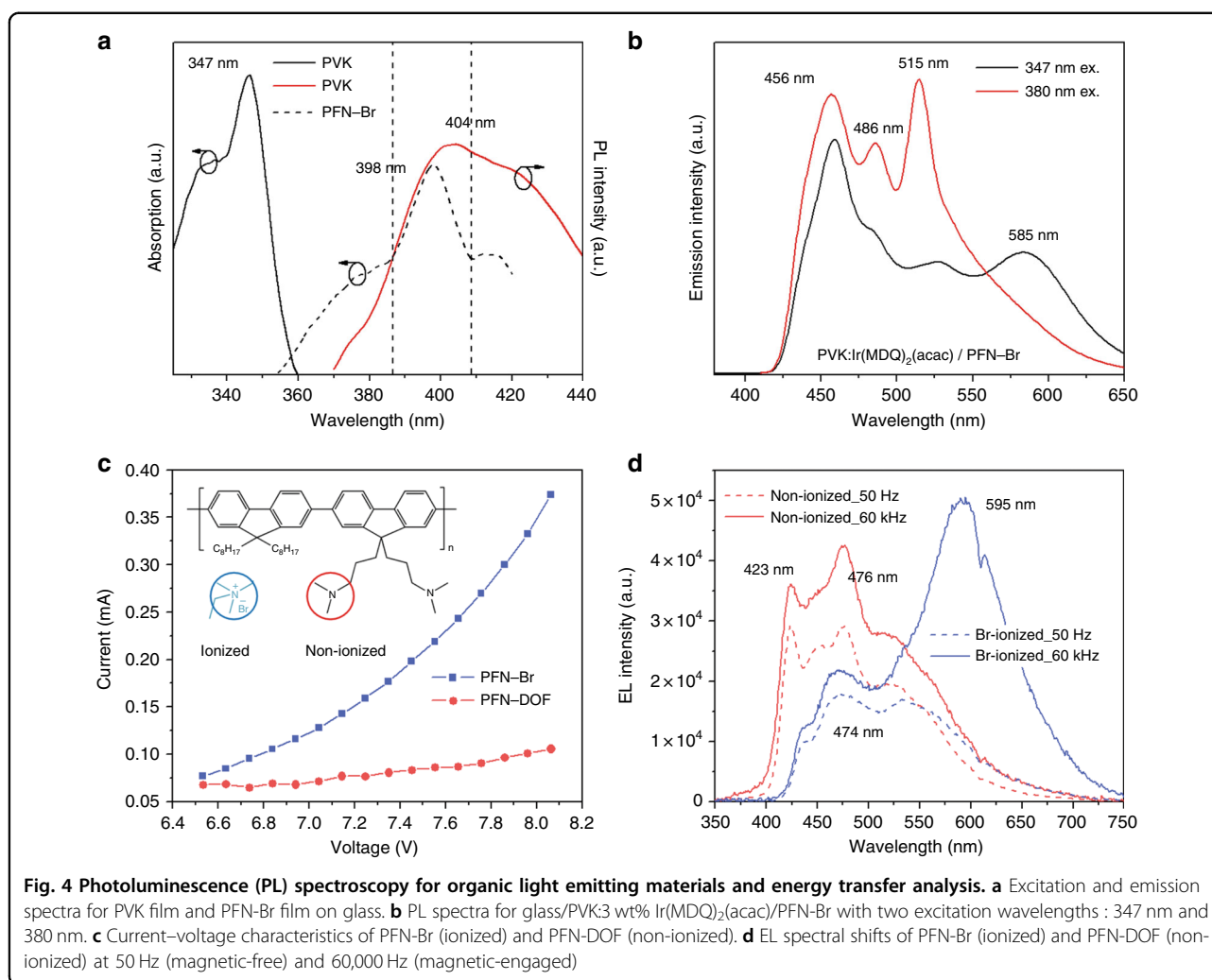
45,000 Hz, which suggests a significantly reduced contribution of hot carrier injection to the total current at high frequency. These opposite trends illustrate that an electric field of $>20,000$ Hz applied to the capacitive device is sufficient to generate a magnetic field that is strong enough to yield secondary charge diffusion. The stronger AC magnetic field (due to higher frequency) suppresses ISC between singlet-state and triplet-state e-h pairs in the PFN-Br, thereby resulting in population enhancement of singlet e-h pairs at the F-P interface. The elevated singlet-triplet ratio promotes the generation of secondary charge carriers. The hopping transport of secondary electrons and holes in the organic semiconductor is acutely tied to the generation of radical triplet excitons in Ir(MDQ)₂(acac), leading to red phosphorescence (as indicated in Fig. 3a). The coupling of the driver to the capacitive device has been taken into consideration by comparing the dominant capacitance of the device (1–3 nF) with the parallel external capacitance (530 pF) in the driver. Driving frequencies of $>50,000$ Hz cause insufficient carrier injection, resulting in the decrease in the number of e-h pairs and the total current reduction in Fig. 3b.

In Fig. 3c, the EL spectrum of the AC-OEL device shows a dramatic color change when the driving field frequency varies from 50; 100; 500; 1000; 10,000; 20,000; 30,000; 40,000; 50,000 Hz, up to 60,000 Hz. The 474 nm emission band is dominant at the low frequency of 50 Hz. As the driving frequency increases, the peaks at 430, 474, and 531 nm (due to PFN-Br's fluorescent emission) are weakened; in contrast, the 595 nm peak (which corresponds to Ir(MDQ)₂(acac)'s phosphorescent emission) grows rapidly and becomes the dominant emission band. All spectra are measured under 100 cd/m², integrated for 500 ms and averaged over 5 runs. The operating pixel images in Fig. 3d provide us with a clearer picture of the color change with frequency in the forward and reverse sweeps. As indicated by the marked circles, the CIE coordinates in Fig. 3e start from (0.23, 0.34) at 50 Hz, cross the white zone, and reach (0.53, 0.40) in the red zone at 60,000 Hz. Another graphic display of the AC-OEL pixel color change with driving frequency is shown in Movie S2. We also observed non-homogenous emission from the pixel, which is mainly attributed to two major mechanisms: the non-homogenous thin film of PFN-Br and the uniformity of the AC magnetic field coupling. The thin PFN-Br layer at the substrate edge has an e-h generation zone close to the F-P interface, which facilitates the drift of the secondary charges, resulting in red emission. The AC field coupling is also spatially dependent, as shown in Fig. 1f, which suggests a stronger magnetic field at the substrate edge than at the center. Therefore, the spatially dependent magnetic field also leads to the red color shift that first occurs in the pixel area near the substrate edge. Further

analysis of the non-homogenous emission can be found in Supplemental Information.

To further study the energy transition at the F-P interface, photoluminescence (PL) spectroscopy is performed, and the results are shown in Fig. 4a, b. The absorption of PFN-Br (peaks at 398 nm) shows a large overlap with the PL spectra of the host PVK (which show a wide peak at 404 nm) in Fig. 4a. This implies an efficient Förster energy transfer route between PVK and PFN-Br (Förster resonance energy transfer efficiency $\sim 21.1\%$, calculated from Figure S8). In the PL spectra for PVK:3 wt % Ir(MDQ)₂(acac)/PFN-Br shown in Fig. 4b, an extra 585 nm peak due to Ir(MDQ)₂(acac) was detected when the sample was excited by 347 nm (PVK's strongest absorption); in contrast, under 380 nm excitation (PFN-Br's strongest absorption), this 585 nm peak is absent. This suggests that direct energy transfer between PFN-Br and Ir(MDQ)₂(acac) is not allowed. The Förster energy transfer from PVK to PFN-Br and the forbidden transfer between PFN-Br and Ir(MDQ)₂(acac) explains the blue fluorescence that is due to PFN-Br in hot carrier injection.

Because of the full ionization of poly[(9,9-bis(3'-(N,N-dimethylamino)propyl)-2,7-fluorene)-alt-2,7-(9,9-dioctylfluorene)] (PFN-DOF) by Br atoms, PFN-Br possesses many moveable negative charges among the main polymers. Figure 4c shows the electron mobility enhancement by the diffusive Br-negative ions compared with PFN-DOF. The ionic conductivity is the most important property of solid polymer electrolyte. By introducing the Br ions into the PFN to form an electrolyte system, the magnitude of the conductivity will be enhanced. The conductivity of PFN-Br ($\sim 7.8 \times 10^{-7}$ S/cm) is significantly improved compared to that of PFN-DOF ($\sim 3.1 \times 10^{-9}$ S/cm), which is due to the Br-anion movements under the electric field. Because of the long-distance diffusion, the movable Br ions are able to populate the free secondary electrons, which leads to the dissociation of more excitons, thereby facilitating carrier diffusion to the phosphorescent emission layer. For comparison with PFN-Br devices, we studied the spectral shift in PFN-DOF devices between a magnetic-field-free device (50 Hz) and an AC-magnetic-field-coupled device (60,000 Hz) in the same architecture. In Fig. 4d, the fluorescence of PFN-DOF (at 423 and 476 nm) is promoted, which implies the promotion of singlet-state excitons by suppressing ISC of PFN-DOF. However, the color change is almost unnoticeable in PFN-DOF, which suggests that the secondary carriers are unable to reach the phosphorescent sites without the aid of Br ions. More work about the magnetic field effect on PFN-DOF can be found in supplementary information and Figure S9. In the absence of a PFN-Br layer, the excitons still can be formed and recombined at the p-n interface. However, the extremely low radiative recombination rate of TPBi facilitates exciton decay



directly at the Ir(MDQ)₂(acac) phosphorescent sites and the PVK fluorescent host, which was demonstrated by the EL spectra in Figure S10.

Discussion

Figure 5a shows the overall energy transfer at the PVK: Ir(MDQ)₂(acac)/PFN-Br heterojunction. There are three processes that must be addressed:

1. ISC of e-h pairs in PFN-Br is magnetic-field-sensitive. In the presence of a magnetic field, energetically inaccessible T⁻ and T⁺ states yield a redistribution of singlet and triplet excited states (S₀: T₀ = 1/2:1/2) in PFN-Br, as has been predicted theoretically⁴¹⁻⁴⁶,
2. Accumulated singlet-spin e-h pairs are dissociated into diffusive secondary carriers with the assistance of Br ions;
3. The energy transfer of e-h pairs between PVK and PFN-Br is efficient but negligible because of the insufficient number of singlet-state excitons in PVK.

The AC magnetic field is only present in the high-frequency electric field. The magnetic field influences the ratio of singlet and triplet spin excitons at the p-n junction where e-h pairs are generated from the injected carriers. As a consequence, the 1:3 singlet-triplet ratio is violated and the singlet spin exciton accumulation occurs in the fluorescent emission layer. In contrast, it is believed that the exciton generation at the p-n interface would not be affected by the AC field due to the constant exciton generation zone.

An instructive and elegant confirmation of the magnetic field effects on F-P tunable emission can be obtained through the use of Fe₃O₄ magnetic NPs as a magnetic field alternative. The nano-magnetite-induced magnetic field is extremely local; hence, it will not introduce extra, unpredicted magnetic field effects as a uniform external magnetic field may do (for instance, possible magnetic field effects on the PVK). Moreover, it has been reported that magnetic field gradients due to Fe₃O₄ nanocrystals are more effective in suppressing ISC processes than static

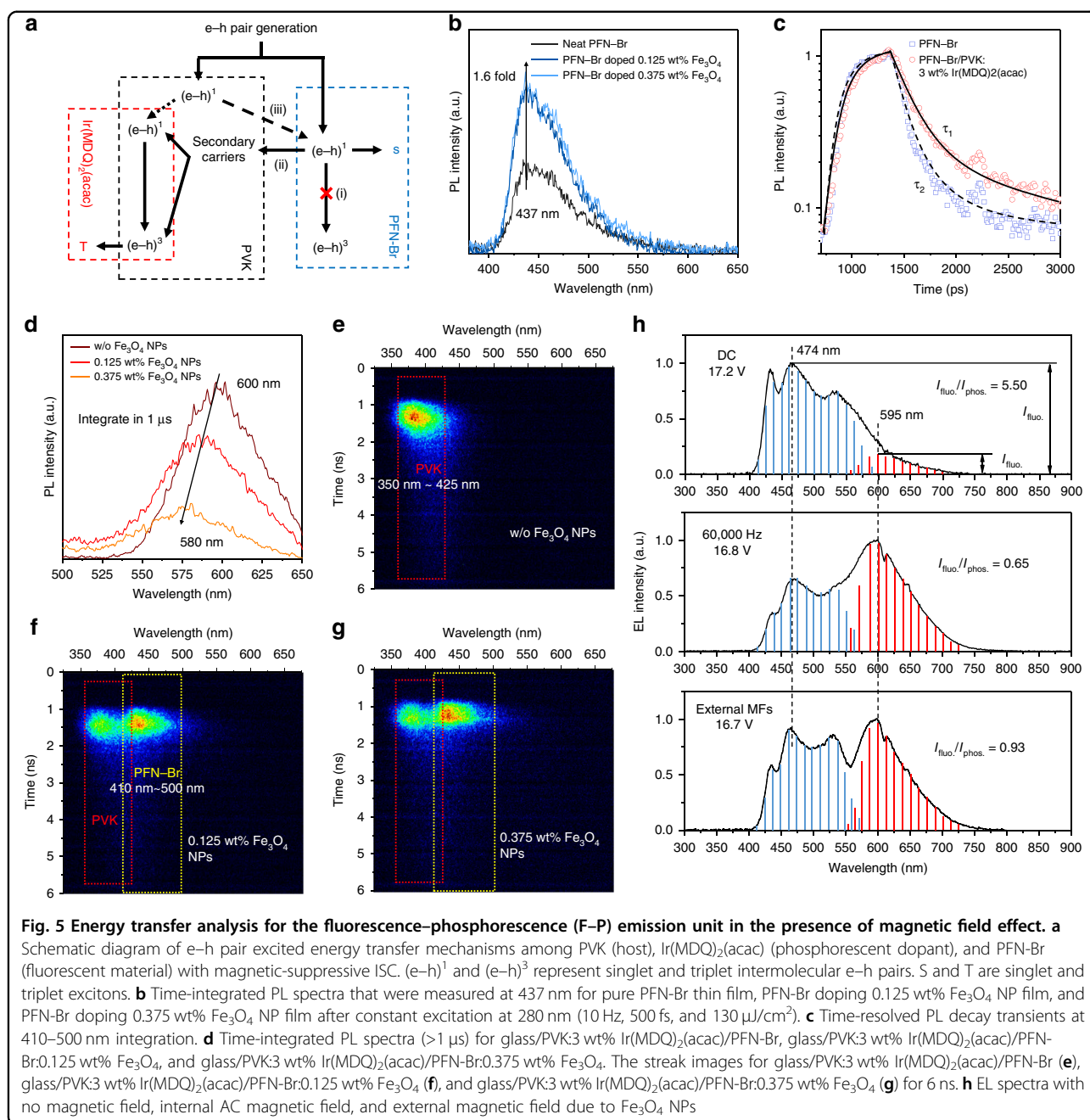


Fig. 5 Energy transfer analysis for the fluorescence-phosphorescence (F-P) emission unit in the presence of magnetic field effect. **a** Schematic diagram of e-h pair excited energy transfer mechanisms among PVK (host), Ir(MDQ)₂(acac) (phosphorescent dopant), and PFN-Br (fluorescent material) with magnetic-suppressive ISC. (e-h)¹ and (e-h)³ represent singlet and triplet intermolecular e-h pairs. S and T are singlet and triplet excitons. **b** Time-integrated PL spectra that were measured at 437 nm for pure PFN-Br thin film, PFN-Br doping 0.125 wt% Fe₃O₄ NP film, and PFN-Br doping 0.375 wt% Fe₃O₄ NP film after constant excitation at 280 nm (10 Hz, 500 fs, and 130 μ J/cm²). **c** Time-resolved PL decay transients at 410–500 nm integration. **d** Time-integrated PL spectra (>1 μ s) for glass/PVK:3 wt% Ir(MDQ)₂(acac)/PFN-Br, glass/PVK:3 wt% Ir(MDQ)₂(acac)/PFN-Br:0.125 wt% Fe₃O₄, and glass/PVK:3 wt% Ir(MDQ)₂(acac)/PFN-Br:0.375 wt% Fe₃O₄. The streak images for glass/PVK:3 wt% Ir(MDQ)₂(acac)/PFN-Br (**e**), glass/PVK:3 wt% Ir(MDQ)₂(acac)/PFN-Br:0.125 wt% Fe₃O₄ (**f**), and glass/PVK:3 wt% Ir(MDQ)₂(acac)/PFN-Br:0.375 wt% Fe₃O₄ (**g**) for 6 ns. **h** EL spectra with no magnetic field, internal AC magnetic field, and external magnetic field due to Fe₃O₄ NPs

external fields for DC devices^{1,42}. The ferromagnetic Fe₃O₄ magnetic NPs used here have an average diameter of 30 nm (Figure S11), which has been demonstrated by the X-ray diffraction (XRD) pattern (Figure S12), and are widely accepted as a ferromagnetic material since superparamagnetic behavior only exists in Fe₃O₄ magnetic NPs with diameters of <10 nm^{47–49}.

The 1.6-fold magnetic-field-enhanced singlet-state excitons in PFN-Br were directly observed in time-integrated PL spectra in Fig. 5b, while 0.125 wt% Fe₃O₄ NPs was doped in PFN-Br. A slight PL intensity increase

is observed in 0.375 wt% Fe₃O₄ NP-doped PFN-Br, indicating the 50% theoretical upper limit of singlet excitons. A constant excitation was used in the experiment: $\lambda_{\text{ex.}} = 280$ nm. In Fig. 5c, we show the picosecond-transient PL intensity of PVK:Ir(MDQ)₂(acac)/PFN-Br ($\tau_1 = 319.7$ ps, where τ_0 is the time required for the PL to fall to 1/e of the initial intensity) and PFN-Br ($\tau_2 = 171.7$ ps) for 410–500 nm emission (which corresponds to PFN-Br's fluorescence). We attribute the PL radiative delay to the short exciton diffusion in PFN-Br, which has a negligible impact on Ir(MDQ)₂(acac)'s phosphorescence. Furthermore, the

relatively reduced PL intensity of Ir(MDQ)₂(acac)'s phosphorescent emission (580 nm–600 nm) in Fig. 5d provides evidence that no diffusive exciton is involved in color tunability even though singlet-state excitons are saturated with doping magnetic NPs in PFN-Br. Therefore, the possibility of diffusive excitons crossing the interface is excluded; in contrast, Br-ion-enhanced secondary carriers are demonstrated. In addition, we analyzed the streak image for the sample of PVK:3 wt% Ir(MDQ)₂(acac)/PFN-Br in Fig. 5e. No emission is observed except for an intense emission band (350–425 nm), which corresponds to PVK's fluorescence. However, PFN-Br's fluorescent emission (410–500 nm) becomes observable when 0.125 wt% Fe₃O₄ (Fig. 5f) or 0.375 wt% Fe₃O₄ (Fig. 5g) are blended into PFN-Br. This result demonstrates that massive numbers of radical singlet-spin pairs are formed in PFN-Br due to the influence of the magnetic field on the F–P emitting unit. Ir(MDQ)₂(acac)'s phosphorescent emission cannot be captured in the first several nanoseconds in either case because of long-lived triplet excitons but appears at 600 nm in time-integrated spectra, as shown in Figure S13.

To confirm the importance of the magnetic effect on the F–P emitting unit, we measured the EL spectra of analogous devices (the device structures are described in detail in Figure S14) in Fig. 5h with zero magnetic field coupling (DC driving), internal AC magnetic field (60,000-Hz driving), and external NP magnetic field (DC driving). A large F–P intensity ratio (I_f/I_p) of 5.5 was observed when the magnetic field was eliminated. In contrast, the F–P intensity ratios are 0.65 and 0.93 in the AC magnetic field and Fe₃O₄ NC magnetic field, respectively. This implies that the low F–P intensity ratio is evidence that secondary charges, which originate from singlet e–h pair accumulation, are able to facilitate the generation of triplet excitons in the Ir(MDQ)₂(acac) molecules.

In summary, the application of internally generated AC magnetic fields in a unique AC-OEL architecture is demonstrated to be an efficient method for manipulating the ratio of singlet- and triplet-spin pairs. The magnetically sensitive ISC can modify the probability of singlet-spin e–h pairs in organics (PFN-Br), which significantly populates diffusive secondary charges to achieve phosphorescence emission (Ir(MDQ)₂(acac)). By varying AC magnetic fields that are coupled at an F–P heterointerface in the AC-OEL device, the emission can be shifted between blue fluorescence (singlet-spin-related) and red phosphorescence (triplet-spin-related) with no significant brightness changes. Conventional contributions to color shifts that are associated with spatial shifting of recombination zones or exciton redistribution and quenching under high voltage have been excluded by our experiments. While the unusual properties of magnetically coupled AC-OEL devices may lead to other breakthrough

devices, our work opens new doors to a more detailed understanding of radical-pair manipulation in the quantum electrodynamics and spintronics of organic materials.

Materials and methods

Materials and device fabrication

The AC-OEL devices were built on a 2.54 × 2.54 cm² glass substrate precoated with a 140-nm-thick layer of ITO with a sheet resistance of ~10 ohms per square. The ITO glass substrate was cleaned in an ultrasonic bath with acetone followed by methanol and isopropanol for 1 h each and dried in vacuum oven for 2 hours. Before spin-coating, the ITO substrates were exposed in UV-ozone for 30 min. To efficiently control the carrier transport under AC driving, PEDOT:PSS doped with 18 wt% ZnO NPs (~35 nm) was spun onto the substrate to form a gate-and-hole-generation layer. For the dual-emission-layer unit, a layer of PVK with 3 wt% Ir(MDQ)₂(acac) was spin-coated in chlorobenzene at a concentration of 10 mg/mL at 2000 rpm, followed by baking at 100 °C for 30 min. The second emission layer was obtained by spin coating the 5 mg/mL (20 nm), 8 mg/mL (50 nm), or 10 mg/mL (70 nm) PFN-Br blends in methanol at 3000 rpm and dried at 95 °C for 20 min. Iron oxide magnetic nanopowder (Fe₃O₄ NPs ~30 nm) was purchased from Sigma-Aldrich and was pre-functionalized by *N*-succinimidyl ester for easy dispersion in a suitable solvent. A 40 nm electron-transport material (TPBi) and a 150 nm top Al electrode were deposited by thermal evaporation through a shadow mask with a 0.16 cm² opening at the rates of 0.2 and 2 Å/s, respectively. Before testing, the devices were sealed by quartz caps with UV curing adhesive in nitrogen atmosphere in a glove box.

Device EL and PL measurement

The AC-OEL devices were measured in ambient air at atmospheric pressure and room temperature (25 °C) with encapsulation. A 200 MHz function/arbitrary waveform generator (Agilent 33220A) connected to an amplifier (Trek PZD700A M/S) provided a sinusoidal signal with suitable voltage and frequency. A power analyzer (Zimmer LMG95) was utilized to read the RMS values of voltage and current on the AC-OEL devices. At the same time, voltage waveforms and current waveforms were recorded by a Tektronix TPS 2024B oscilloscope to validate the voltage and current values. The method that we used to determine the AC and DC current components is described in detail in Supplemental Information. A photometer (ILT 1400-A) was used to measure the out-coupling luminance. The entire system was connected and controlled by a computer. To obtain accurate and reliable measurements of luminance, each turn-on measurement of the pixels was integrated over 2000 ms and averaged 5 times instead of fast sweeping to yield good-looking curves. The EL spectra for color-tunable AC-OEL

devices were collected by an ILT 950 spectroradiometer (International Light Technologies) while the driving frequency was varied easily by a function waveform generator. The PL spectra for PVK, PFN-Br, and PVK:Ir (MDQ)₂(acac)/PFN-Br thin films were measured by a fluorescence spectrometer (PerkinElmer LS50B).

Streak camera test

For measurement of the transient PL characteristics, short-pulse excitation with a pulse width of 200 fs and a wavelength of 280 nm was used in combination with a Hamamatsu C2830 streak camera system that mainly consisted of a C2830 streak camera and an M2547 fast sweep unit (resolution <10 ps). F–P lifetime measurements were carried out via a photodiode with UV laser illumination in dark-room ambient at 25 °C.

Transmission electron microscopy (TEM) and atomic force microscopy (AFM) images

A TEM (JEOL JEM-1200EX) was utilized to analyze the morphology of Fe₃O₄ NPs dispersed in PFN-Br methanol solution. The surface morphology analyses of PVK and PFN-Br were performed using an AFM (Asylum Research MFP-3D-BIO).

X-ray diffraction (XRD) pattern

The crystalline phase analysis was performed using an X-ray powder diffractometer (Bruker D2 PHASER) in ambient. The result was averaged over 10 measurements.

Acknowledgements

We thank Prof. R.T. Williams, D.R. Onken, and Dr. K.B. Ucer for access to the streak camera in Olin laboratory at Wake Forest University. We acknowledge H. Lee for assistance with the atomic force microscopy test. We thank Dr. Y. Zheng for help with the XRD test. We acknowledge the financial support and use of equipment from the Center for Nanotechnology and Molecular Materials at Wake Forest University. Research funding was also provided through NSF grant ECCS-1610641.

Author details

¹Center for Nanotechnology and Molecular Materials, Wake Forest University, Winston-Salem, NC 27109, USA. ²Department of Physics, Wake Forest University, Winston-Salem, NC 27106, USA. ³Key Laboratory of Luminescence and Optical Information (Ministry of Education), Institute of Optoelectronics Technology, Beijing Jiaotong University, 100044 Beijing, P.R. China. ⁴Department of Electro-Optics, School of Engineering, University of Dayton, Dayton, OH 45469, USA. ⁵Department of Mathematics, Wake Forest University, Winston-Salem, NC 27106, USA. ⁶State Key Laboratory for Modification of Chemical Fibers and Polymer Materials, 201620 Shanghai, P.R. China. ⁷College of Materials Science and Engineering, Donghua University, 201620 Shanghai P.R. China. ⁸Institute of Advanced Materials, Nanjing Tech University, 211816 Nanjing, Jiangsu, P.R. China. ⁹Present address: Department of Physics and Astronomy, College of Charleston, Charleston, SC 29424, USA

Author contributions

J.X. and D.C. designed the experiments and performed the theoretical analysis. J.X. fabricated and tested the devices and performed the data analysis. J.X. and Y.C. carried out the photoluminescence test and performed the energy transfer mechanism analysis. G.S. prepared the materials used in this work and maintained the equipment. J.X. and P.L. performed the streak camera test and transient photoluminescence analysis. C.D. and J.X. conducted the microscope

and XRD analyses. J.X. and L.S. optimized the performance of the color-tunable AC-OEL pixels. J.X., Y.G., H.W., and Y.C. discussed the results. J.X. and D.C. wrote the paper. D.C. planned and supervised the entire project. All authors discussed the results and reviewed the manuscript.

Conflict of interest

The authors declare that they have no conflict of interest.

Supplementary information is available for this paper at <https://doi.org/10.1038/s41377-018-0046-5>.

Received: 7 February 2018 Revised: 4 June 2018 Accepted: 5 June 2018

Accepted article preview online: 27 June 2018

Published online: 01 August 2018

References

- Tang, C. W. & VanSlyke, S. A. Organic electroluminescent diodes. *Appl. Phys. Lett.* **51**, 913–915 (1987).
- Friend, R. H. et al. Electroluminescence in conjugated polymers. *Nature* **397**, 121–128 (1999).
- Pope, M., Kallmann, H. P. & Magnante, P. Electroluminescence in organic crystals. *J. Chem. Phys.* **38**, 2042–2043 (1963).
- Baldo, M. A., O'Brien, D. F., Thompson, M. E. & Forrest, S. R. Excitonic singlet-triplet ratio in a semiconducting organic thin film. *Phys. Rev. B* **60**, 14422–14428 (1999).
- Adachi, C., Baldo, M. A., Thompson, M. E. & Forrest, S. R. Nearly 100% internal phosphorescence efficiency in an organic light-emitting device. *J. Appl. Phys.* **90**, 5048–5051 (2001).
- Baldo, M. A. et al. Highly efficient phosphorescent emission from organic electroluminescent devices. *Nature* **395**, 151–154 (1998).
- Kawamura, Y. et al. 100% phosphorescence quantum efficiency of Ir (III) complexes in organic semiconductor films. *Appl. Phys. Lett.* **86**, 071104 (2005).
- Forget, S. & Chénais, S. *Organic Solid-State Lasers* (Springer, Berlin, Heidelberg, 2013).
- Bobbert, P. A. Manipulating spin in organic spintronics. *Science* **345**, 1450–1451 (2014).
- Hu, B. & Wu, Y. Tuning magnetoresistance between positive and negative values in organic semiconductors. *Nat. Mater.* **6**, 985–991 (2007).
- Nguyen, T. D., Gautam, B. R., Ehrenfreund, E. & Vardeny, Z. V. Magnetoconductance response in unipolar and bipolar organic diodes at ultrasmall fields. *Phys. Rev. Lett.* **105**, 166804 (2010).
- Bobbert, P. A., Nguyen, T. D., van Oost, F. W. A., Koopmans, B. & Wohlgenannt, M. Bipolaron mechanism for organic magnetoresistance. *Phys. Rev. Lett.* **99**, 216801 (2007).
- Wu, Y., Xu, Z. H., Hu, B. & Howe, J. Tuning magnetoresistance and magnetic-field-dependent electroluminescence through mixing a strong-spin-orbital-coupling molecule and a weak-spin-orbital-coupling polymer. *Phys. Rev. B* **75**, 035214 (2007).
- Mahato, R. N. et al. Ultrahigh magnetoresistance at room temperature in molecular wires. *Science* **341**, 257–260 (2013).
- Prigodin, V. N., Bergeson, J. D., Lincoln, D. M. & Epstein, A. J. Anomalous room temperature magnetoresistance in organic semiconductors. *Synth. Met.* **156**, 757–761 (2006).
- Janssen, P. et al. Tuning organic magnetoresistance in polymer-fullerene blends by controlling spin reaction pathways. *Nat. Commun.* **4**, 2286 (2013).
- Kalinowski, J., Szymkowski, J. & Stampor, W. Magnetic hyperfine modulation of charge photogeneration in solid films of Alq₃. *Chem. Phys. Lett.* **378**, 380–387 (2003).
- Wilkinson, J., Davis, A. H., Bussmann, K. & Long, J. P. Evidence for charge-carrier mediated magnetic-field modulation of electroluminescence in organic light-emitting diodes. *Appl. Phys. Lett.* **86**, 111109 (2005).
- Müller, J. G. et al. Ultrafast dynamics of charge carrier photogeneration and geminate recombination in conjugated polymer: fullerene solar cells. *Phys. Rev. B* **72**, 195208 (2005).
- Szymkowski, J., Stampor, W., Kalinowski, J. & Kafafi, Z. H. Electric field-assisted dissociation of singlet excitons in tris-(8-hydroxyquinolino) aluminum (III). *Appl. Phys. Lett.* **80**, 1465 (2002).

21. Stampo, W. Electromodulation of fluorescence in hole-transporting materials (TPD, TAPC) for organic light-emitting diodes. *Chem. Phys.* **256**, 351–362 (2000).
22. Kalinowski, J. et al. Coexistence of dissociation and annihilation of excitons on charge carriers in organic phosphorescent emitters. *Phys. Rev. B* **74**, 085316 (2006).
23. Wittmer, M. & Zschokke-Gränacher, I. Exciton–charge carrier interactions in the electroluminescence of crystalline anthracene. *J. Chem. Phys.* **63**, 4187–4194 (1975).
24. Tolstov, I. V. et al. On the role of magnetic field spin effect in photoconductivity of composite films of MEH-PPV and nanosized particles of PbS. *J. Lumin.* **112**, 368–371 (2005).
25. Levinson, J., Weisz, S. Z., Cobas, A. & Rolón, A. Determination of the triplet exciton-trapped electron interaction rate constant in anthracene crystals. *J. Chem. Phys.* **52**, 2794–2795 (1970).
26. Shen, Z. L., Burrows, P. E., Bulović, V., Forrest, S. R. & Thompson, M. E. Three-color, tunable, organic light-emitting devices. *Science* **276**, 2009–2011 (1997).
27. Fröbel, M. et al. Get it white: color-tunable AC/DC OLEDs. *Light Sci. Appl.* **4**, e247 (2015).
28. Berggren, M. et al. Light-emitting diodes with variable colours from polymer blends. *Nature* **372**, 444–446 (1994).
29. Al Attar, H. A., Monkman, A. P., Tavasli, M., Bettington, S. & Bryce, M. R. White polymeric light-emitting diode based on a fluorene polymer/Ir complex blend system. *Appl. Phys. Lett.* **86**, 121101 (2005).
30. Parthasarathy, G., Gu, G. & Forrest, S. R. A full-color transparent metal-free stacked organic light emitting device with simplified pixel biasing. *Adv. Mater.* **11**, 907–910 (1999).
31. Xu, J. W., Carroll, D. L., Smith, G. M., Dun, C. C. & Cui, Y. Achieving high performance in AC-field driven organic light sources. *Sci. Rep.* **6**, 24116 (2016).
32. Xu, J. W. et al. Layered, nanonetwork composite cathodes for flexible, high-efficiency, organic light emitting devices. *Adv. Funct. Mater.* **25**, 4397–4404 (2015).
33. Chen, Y. H., Xia, Y. D., Smith, G. M. & Carroll, D. L. Frequency-dependent, alternating current-driven, field-induced polymer electroluminescent devices with high power efficiency. *Adv. Mater.* **26**, 8133–8140 (2014).
34. Perumal, A. et al. Novel approach for alternating current (AC)-driven organic light-emitting devices. *Adv. Funct. Mater.* **22**, 210–217 (2012).
35. Tian, Y., Xu, X. J., Wang, J. S., Yao, C. & Li, L. D. Solution-processed white organic light-emitting diodes with enhanced efficiency by using quaternary ammonium salt doped conjugated polyelectrolyte. *ACS Appl. Mater. Interfaces* **6**, 8631–8638 (2014).
36. Huang, F., Wu, H. B., Wang, D. L., Yang, W. & Cao, Y. Novel electroluminescent conjugated polyelectrolytes based on polyfluorene. *Chem. Mater.* **16**, 708–716 (2004).
37. Khramtchenkov, D. V., Arkhipov, V. I. & Bässler, H. Charge carrier recombination in organic bilayer electroluminescent diodes. I. Theory. *J. Appl. Phys.* **81**, 6954–6962 (1997).
38. Jonda, C. & Mayer, A. B. R. Investigation of the electronic properties of organic light-emitting devices by impedance spectroscopy. *Chem. Mater.* **11**, 2429–2435 (1999).
39. Pingree, L. S. C., Scott, B. J., Russell, M. T., Marks, T. J. & Hersam, M. C. Negative capacitance in organic light-emitting diodes. *Appl. Phys. Lett.* **86**, 073509 (2005).
40. Luo, H. W. et al. Remarkable enhancement of charge carrier mobility of conjugated polymer field-effect transistors upon incorporating an ionic additive. *Sci. Adv.* **2**, e1600076 (2016).
41. Wang, J. P., Chepelianskii, A., Gao, F. & Greenham, N. C. Control of exciton spin statistics through spin polarization in organic optoelectronic devices. *Nat. Commun.* **3**, 1191 (2012).
42. Cohen, A. E. Nanomagnetic control of intersystem crossing. *J. Phys. Chem. A* **113**, 11084–11092 (2009).
43. Manolopoulos, D. E. & Hore, P. J. An improved semiclassical theory of radical pair recombination reactions. *J. Chem. Phys.* **139**, 124106 (2013).
44. Thomas, J. K. Excited states and reactions in liquids. *Ann. Rev. Phys. Chem.* **21**, 17–38 (1970).
45. Ding, B. F. et al. Magnetic field modulated exciton generation in organic semiconductors: an intermolecular quantum correlated effect. *Phys. Rev. B* **82**, 205209 (2010).
46. Song, J. Y., Stingelin, N., Drew, A. J., Kreouzis, T. & Gillin, W. P. Effect of excited states and applied magnetic fields on the measured hole mobility in an organic semiconductor. *Phys. Rev. B* **82**, 085205 (2010).
47. Caruntu, D., Caruntu, G. & O'Connor, C. J. Magnetic properties of variable-sized Fe₃O₄ nanoparticles synthesized from non-aqueous homogeneous solutions of polyols. *J. Phys. D Appl. Phys.* **40**, 5801–5809 (2007).
48. Goya, G. F. et al. Magnetic hyperthermia with Fe₃O₄ nanoparticles: the influence of particle size on energy absorption. *IEEE Trans. Magn.* **44**, 4444–4447 (2008).
49. Iida, H., Takayanagi, K., Nakanishi, T. & Osaka, T. Synthesis of Fe₃O₄ nanoparticles with various sizes and magnetic properties by controlled hydrolysis. *J. Colloid Interface Sci.* **314**, 274–280 (2007).